

Fluorinated sodiophilic interphase for high-rate and low-temperature initially anode-free sodium battery

Received: 27 June 2025

Accepted: 19 November 2025

Published online: 05 December 2025

Check for updates

Mingxu Wang¹, Jinyu Yang¹, Haoran Ji¹, Ziyue Li¹ , Fengmei Wang¹, Fang Fang^{1,2} , Jiafeng Ruan^{1,3} , Dalin Sun¹ & Fei Wang^{1,4}

Sodium-ion batteries are promising as next-generation energy storage batteries, while suffer from the limited energy density. Initially anode-free sodium batteries effectively alleviate this predicament, but they are primarily hindered by uneven plating/stripping behavior, especially at high rates and low temperatures. Herein, we propose a fluorinated sodiophilic interphase towards high-rate and low-temperature initially anode-free sodium batteries. Systemically comparison between various interphase reveals that Na-alloying-metal containing interphase with high Na adsorption energy and low lattice mismatch facilitates uniform spherical Na plating under high current densities. Besides that, the in-situ formed sodium fluoride strengthens the mechanical properties of the interphase and regulates Na deposition. The optimized BiF₃-derived interphase enables stable Na plating/stripping for over 2800 hours with an average Coulombic efficiency of 99.90%, high-rate capability at 20 mA cm⁻², and low-temperature adaptability at -30 °C. Coupled with Na₄Fe₃(PO₄)₂P₂O₇ positive electrode, initially anode-free full batteries deliver specific powers of 8257.5 W kg⁻¹ at 25 °C and 486.9 W kg⁻¹ at -30 °C (based on the mass of active materials). The assembled pouch-cell operate stably at a high rate of 7 C (1 C = 100 mA g⁻¹). This work provides a strategic framework for advancing initially anode-free sodium battery technology.

Sodium-ion batteries (SIBs) have emerged as promising alternatives to lithium-ion batteries (LIBs) due to the abundance of sodium resources and enhanced safety, while their widespread adoption is hindered by the relative low energy density^{1,2}. Initially anode-free sodium batteries (AFSBs), which eliminates the conventional hard carbon negative electrode and minimizes electrolyte usage, represent a transformative paradigm for maximizing energy density in sodium-based energy storage systems (Fig. 1a)^{3,4}. Nevertheless, the initially anode-free configuration relies on Na plating/stripping onto the current collector, which suffers from inherently sluggish kinetics. Moreover, the fragile solid electrolyte interphase (SEI) on the negative electrode current

collector undergoes repeated cracking and restructuring during heterogeneous Na plating/stripping, exacerbating capacity degradation^{5,6}. Under high current density or low temperature conditions, increased polarization and intensified sodium dendrite growth severely compromise plating/stripping reversibility^{3,7}. To date, a substantial performance gap persists between initially anode-free batteries and state-of-the-art SIBs in terms of high-power adaptability (Fig. 1b)⁸⁻²⁶. Various current collector modifiers such as 3D host materials^{16,17}, sodiophilic metals^{5,19,22} and artificial SEI^{13,18} for durable AFSBs have been explored recent years, and several electrolyte regulation and separator engineering strategies have also been

¹College of Smart Materials and Future Energy, Fudan University, Shanghai, PR China. ²Yiwu Research Institute of Fudan University, Yiwu, PR China. ³Inorganic Chemistry I, Technische Universität Dresden, Dresden, Germany. ⁴Shanghai Key Laboratory of Molecular Catalysis and Innovative Materials, Fudan University, Shanghai, PR China. e-mail: rjfeng@fudan.edu.cn; dlsun@fudan.edu.cn; feiw@fudan.edu.cn

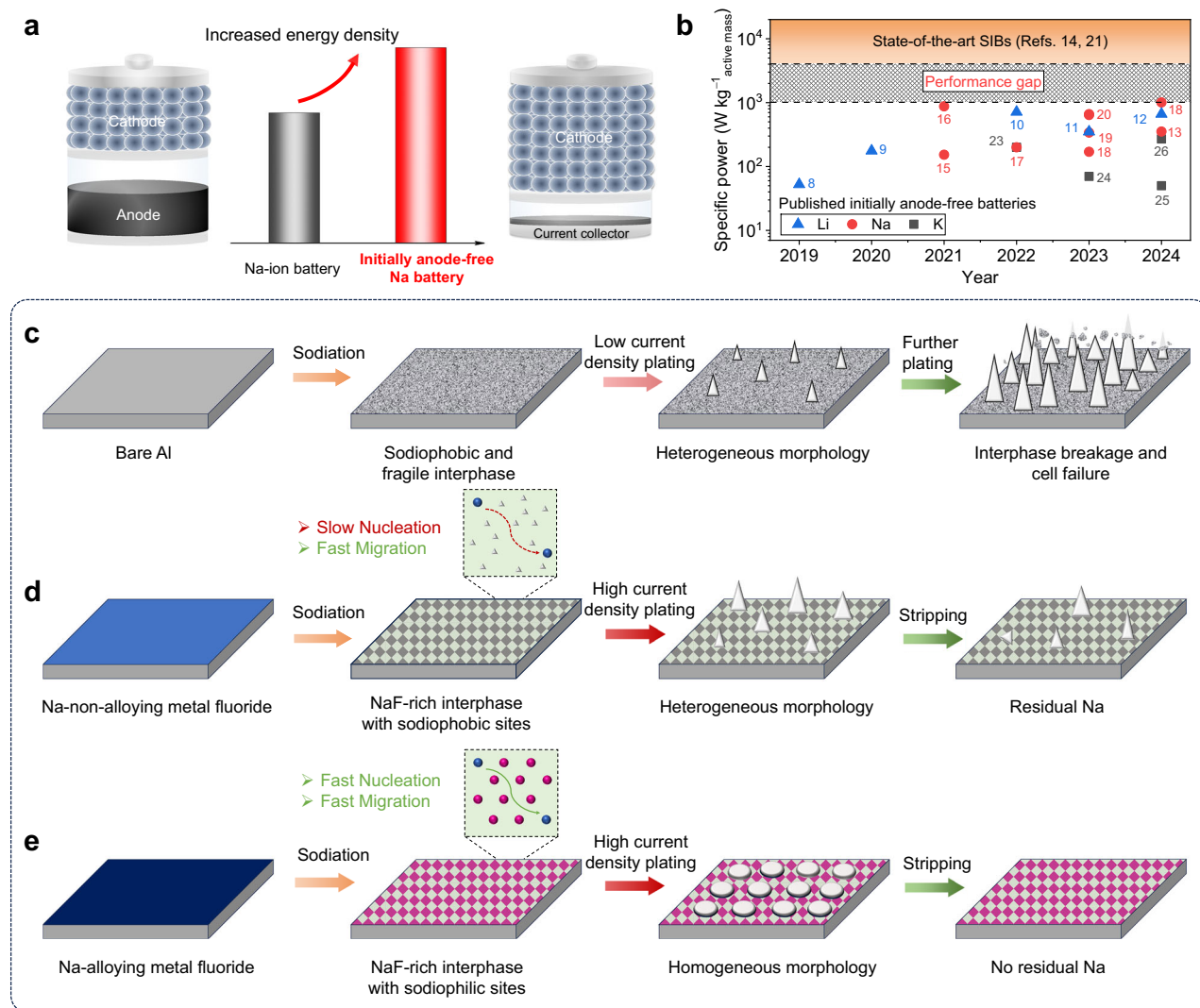


Fig. 1 | Fluorinated Sodiophilic Interphase Design for high-rate initially anode-free sodium battery. **a** Configurations of Na-ion battery and initially anode-free Na battery and the comparisons of energy densities. **b** Comparisons of power densities

of published initially anode-free alkali-metal batteries with state-of-the-art SIBs. Schematic illustrations of sodiation and Na plating/stripping behavior on bare Al (**c**), Na-non-alloying metal fluorides (**d**) and Na-alloying metal fluorides (**e**).

proposed^{7,27–30}. Nevertheless, AFSBs with specific powers exceeding 10^3 W kg^{-1} remain rare, and the interphase design criterion towards high-power AFSBs is still lacking. Moreover, AFSBs for low-temperature scenarios were seldomly reported. Interphase for high-power and low-temperature AFSBs has thus become significant research frontier, with the potential to unlock the full potential of this promising technology.

In this work, various metal fluorides were selected and coated onto Al current collector (noted as $\text{MF}_x@Al$). As shown in Fig. 1c, fragile SEI forms on bare Al at initial sodiation, and plated Na shows heterogeneous morphology under the low current density. Further plating might break the interphase and deteriorate the battery performance. $\text{MF}_x@Al$ current collectors benefit both mechanical property and interphasial sodiophilicity, while the durability at high current densities depends on the selection of metal element. The Na-non-alloying metal fluorides derived interphase exhibits low affinity for Na, resulting in irreversible Na loss at high current densities (Fig. 1d). In contrast, the sodiophilic interphase derived from Na-alloying metal promotes homogeneous Na plating, thereby significantly improving battery performance at high current densities (Fig. 1e). The optimized BiF_3 -derived interphase exhibits fast kinetics and high reversibility.

Consequently, the $\text{BiF}_3@Al$ current collector not only achieves stable Na plating/stripping for over 2800 h with an average Coulombic efficiency (CE) of 99.90% but also demonstrates high-rate capability of 20 mA cm^{-2} and low-temperature adaptability at -30°C . Furthermore, the $\text{BiF}_3@Al||\text{Na}_4\text{Fe}_3(\text{PO}_4)_2\text{P}_2\text{O}_7$ full batteries exhibit a specific power of 8257.5 W kg^{-1} (with a specific energy of 112.4 Wh kg^{-1}) at 25°C and 486.9 W kg^{-1} (80.7 Wh kg^{-1}) at -30°C . The full batteries exhibit extended cycle stability (over 1600 cycles) at 1 C and -30°C . The assembled $\text{BiF}_3@Al||\text{Na}_4\text{Fe}_3(\text{PO}_4)_2\text{P}_2\text{O}_7$ pouch cells demonstrated stable operation at the high rate of 7 C. This work provides valuable insights for interphase design towards high-power AFSBs, and sheds light on their future development.

Results

Effect of the in-situ conversion products of metal fluorides

To investigate the impact of metal elements of the fluorides on Na nucleation and growth behavior, six metal fluorides were selected and coated on the aluminum current collector, three of which cannot be alloyed with Na (FeF_3 , CoF_2 , and NiF_2) and others can be alloyed with Na (ZnF_2 , SnF_2 , and BiF_3), as shown in Fig. 2a. $\text{Na}||\text{MF}_x@Al$ cells were assembled and tested at $1 \text{ mA cm}^{-2}@1 \text{ mAh cm}^{-2}$ in an ether-based

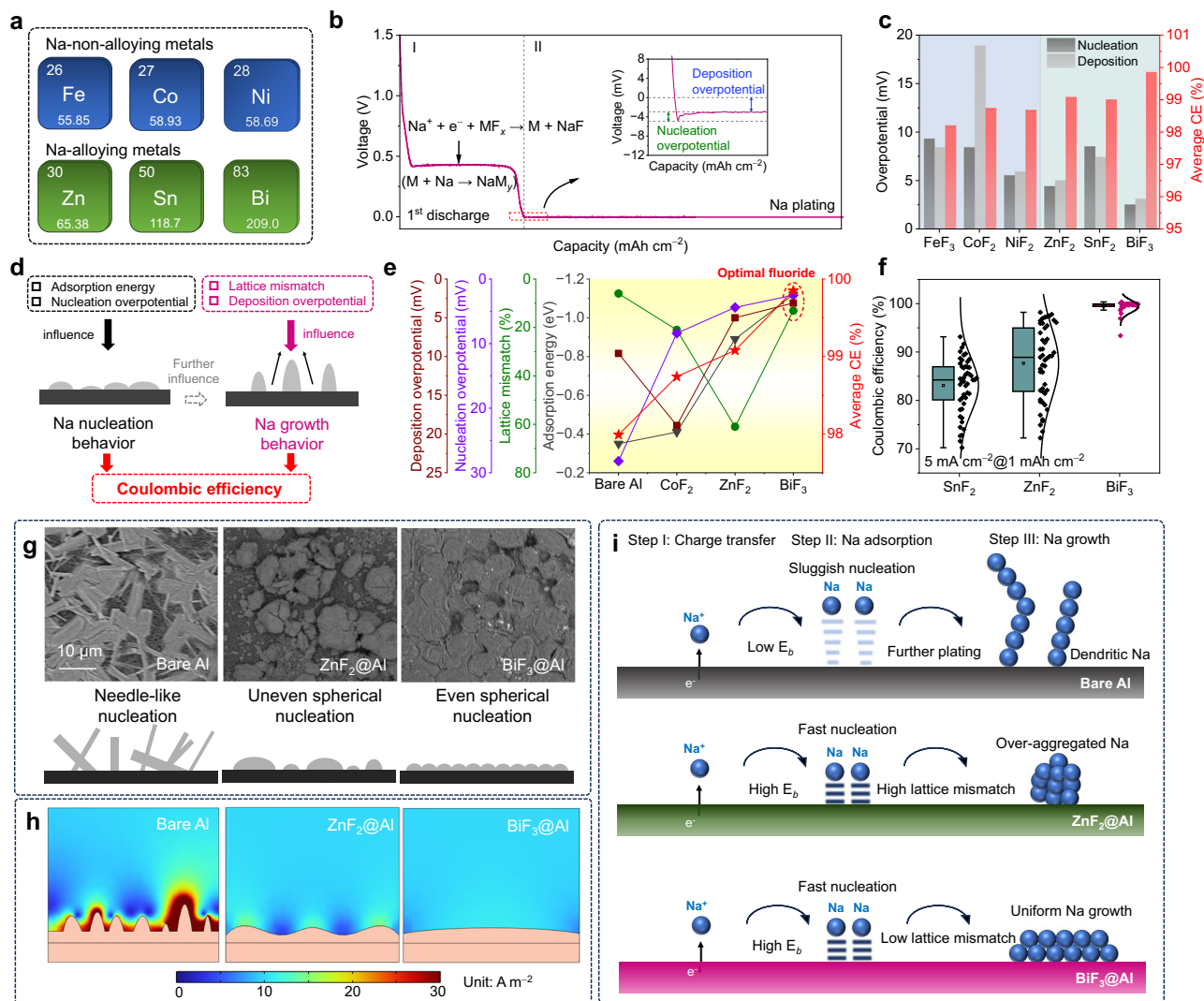


Fig. 2 | Effect of metal-fluoride-derived interphase on Na plating behavior. **a** Selection of metal elements for two classes of fluoride materials. **b** Voltage profile of metal fluorides during the first discharge process at 25 °C and the reaction equation. Inset: enlarged curve near 0 V. **c** Comparisons of nucleation overpotential, deposition overpotential, and average CE of the 2nd to 100th cycles of Na plating/stripping at 1 mA cm⁻²@1 mA h cm⁻² of Na||MF_x@Al at 25 °C. **d** Schematic illustration of the influencing factors of CE in anode-free batteries. **e** Comparisons of lattice mismatch, adsorption energy, nucleation overpotential, deposition overpotential, and average CE of the 2nd to 100th cycles at 1 mA cm⁻²@1 mA h cm⁻² of

bare Al, CoF₂@Al, ZnF₂@Al, and BiF₃@Al. **f** Comparisons of the distributions of CE from 2nd to 50th cycles at 5 mA cm⁻²@1 mA h cm⁻² of SnF₂@Al, ZnF₂@Al, and BiF₃@Al at 25 °C. Data are presented as mean values ± SD. 49 values are used to derive the SD. **g** Top-view SEM images and schematic illustrations of 0.2 mA h cm⁻² of Na plating at 25 °C on bare Al, ZnF₂@Al and BiF₃@Al at a high current density of 10 mA cm⁻². **h** Simulated current density distribution on bare Al, ZnF₂@Al, and BiF₃@Al at a current density of 1 mA cm⁻² via COMSOL. **i** Schematic illustration of the Na plating process on bare Al, ZnF₂@Al and BiF₃@Al.

electrolyte (1.0 M NaPF₆-diglyme) owing to its high stability on Na metal and low-temperature adaptability, as the ester-based electrolyte shows poor stability in initially anode-free system (Supplementary Fig. 1). Figure 2b shows the typical voltage profile of a metal fluoride during the first discharge process. In Region I, a plateau at about 0.5 V is ascribed to the in-situ electrochemical reaction between MF_x and Na⁺ below:



After that, the voltage rapidly drops below 0 V, followed by the emergence of an extended plateau slightly below 0 V in Region II, corresponding to the Na nucleation and deposition processes. In the inset of Fig. 2b, the voltage hysteresis of the discharge curve is noted as nucleation overpotential, and the plateau voltage of Region II is noted

as deposition overpotential. Clearly, a lower nucleation and deposition overpotential facilitates uniform Na deposition and subsequent efficient stripping, which is expected to achieve a high CE. The overpotentials and average CEs between 2 and 100 cycles of metal fluorides are shown in Fig. 2c and Supplementary Fig. 2. Metals which can be alloyed with Na show lower overpotentials and higher average CEs. Among them, BiF₃@Al exhibits the lowest nucleation and deposition overpotential (2.5 and 3.1 mV), suggesting favorable Na nucleation and uniform growth. As expected, BiF₃@Al displays the highest average CE of 99.85%. Therefore, we preliminarily screened out BiF₃ as the optimal metal fluoride modifier for AFSBs.

To further prove this result and verify its consistency under high current densities, multiple factors influencing Na nucleation and growth are taken into account. In Fig. 2d, Na nucleation behavior on the modified current collector is influenced by the Na adsorption energy on the electrolyte-electrode interphase and the nucleation

overpotential. Furthermore, Na growth behavior is determined by the lattice mismatch between Na and the interphase, as well as the deposition overpotential. The interplay between Na nucleation and growth behavior ultimately dictates the cycling performance of AFSBs^{17,31}. Density functional theory (DFT) calculations reveal the Na adsorption sites and adsorption energy (E_b) on various fluoride-derived interphases (Supplementary Fig. 3 and Supplementary Data 1), while the lattice mismatch is calculated using the following equation:

$$\delta = \frac{|a_M - a_{Na}|}{a_M} \quad (2)$$

where a_{Na} and a_M are the lattice constant of Na and the metal, respectively. For Na-alloying metals, a_M is placed by a_{NaM} , such as $a_{NaZn_{13}}$ and a_{Na_3Bi} . Comparative results are summarized in Fig. 2e. Specifically, although Na exhibits a low lattice mismatch (~6%) with Al, it shows a low E_b of only -0.35 eV, indicating poor sodiophilicity. As a result, bare Al exhibits the highest nucleation overpotential and a low average CE of -97.9%. Similar to the phenomenon observed with bare Al, $CoF_2@Al$ exhibits high nucleation and deposition overpotentials, primarily due to its sodiophobic nature. Fortunately, the formation of a NaF-rich interphase derived by CoF_2 improves the CE of Na plating/stripping. In contrast, Zn, which can alloy with Na, shows a higher sodiophilicity ($E_b = -0.89$ eV on $NaZn_{13}$). However, its Na plating/stripping reversibility is still inadequate due to the huge lattice mismatch of Na with $NaZn_{13}$ (~61%). Among all selected metal fluorides, BiF_3 -derived interphase exhibits the highest sodiophilicity ($E_b = -1.12$ eV on Na_3Bi), low lattice mismatch (13.1%), and the lowest overpotential, hence shows the highest average CE. Even when the current density increases to 5 mA cm^{-2} , $BiF_3@Al$ still exhibits a high average CE of 99.75%, while other five fluorides suffer from severe CE fluctuations (Fig. 2f and Supplementary Fig. 4). In Supplementary Fig. 5, only $BiF_3@Al$ remains stable for over 300 cycles at higher current density of 10 mA cm^{-2} , while $ZnF_2@Al$ exhibits more severe CE fluctuations and other four fluorides fail within several cycles. Notably, the voltage profiles of “CE > 100%” cells are shown in Supplementary Fig. 6, where the voltage fluctuation during charging process indicates the cell soft short-circuit during Na stripping. In Supplementary Fig. 7, $BiF_3@Al$ still maintains stable even at 20 and 30 mA cm^{-2} . Overall, BiF_3 demonstrates its potential as an interphase modifier for high-power AFSBs.

Na nucleation morphology has a profound impact on Na plating/stripping reversibility, and it generally deteriorates under high current density¹¹. Therefore, scanning electron microscopy (SEM) is employed to visualize the morphology of plated Na. The current densities were set as 10 and 1 mA cm^{-2} , respectively, and the Na plating capacity was set as 0.2 mAh cm^{-2} . In Supplementary Fig. 8a, b, needle-like Na is observed on bare Al and $CoF_2@Al$ (metals cannot be alloyed with Na), which might lead to dendritic Na and deteriorate the Na plating/stripping reversibility. This phenomenon becomes more pronounced as the current density increases to 10 mA cm^{-2} . In Fig. 2g and Supplementary Fig. 9a, the Na nuclei become sharper and more voids are observed on bare Al and $CoF_2@Al$, suggesting sluggish nucleation kinetics. In contrast, spherical Na is observed on $ZnF_2@Al$ and $BiF_3@Al$ (metals can be alloyed with Na), as shown in Fig. 2g and Supplementary Fig. 8c, d. Notably, the spherical Na on the $BiF_3@Al$ are uniform at both 1 and 10 mA cm^{-2} , while the Na nuclei on ZnF_2 seem to grow unevenly and collapse at high current density, which might be ascribed to the huge lattice mismatch between Na and $NaZn_{13}$. These results suggest the advantage of BiF_3 -derived interphase on boosting Na nucleation and inducing Na even plating kinetics. The advantage of the BiF_3 in facilitating fast and reversible Na plating/stripping was further investigated by finite element analysis (FEA), as shown in Fig. 2h and Supplementary Fig. 9b. The color variations denote differences in current density. On bare Al and $CoF_2@Al$, the current densities are notably

concentrated at surface protrusions, leading to uneven Na nucleation and promoting Na dendrite growth. In contrast, the current density distributions on $ZnF_2@Al$ and $BiF_3@Al$ are more uniform, indicating that Zn- and Bi-contained interphase can homogenize the current density distribution, thereby facilitating even Na nucleation. Between this group, $BiF_3@Al$ shows the most uniform current density distribution, which further confirming its effectiveness in achieving uniform Na nucleation morphology. As summarized in Fig. 2i, Na suffers from sluggish nucleation process on bare Al, which leads to dendritic Na growth. Na-alloying-metal-rich interphase accelerates Na nucleation owing to the increased E_b , while Na tends to over-aggregate due to huge lattice mismatch between Na and ZnF_2 -derived interphase. On the contrary, BiF_3 -derived interphase facilitates fast nucleation and uniform Na growth benefiting from high E_b and low lattice mismatch.

The electrochemical performance of AFSBs is largely dependent upon the properties of SEI, especially under high current density. Thus, the composition and properties of the SEI were systematically analyzed in order to investigate the regulatory effect of the BiF_3 -derived interphase on Na growth, as shown in Fig. 3. X-ray photoelectron spectroscopy (XPS) analysis with depth profiling was employed to analyze the chemical composition of SEI formed on bare Al and $BiF_3@Al$ surface after 20 cycles of Na plating/stripping at a high current density of 10 mA cm^{-2} . In Fig. 3a, b, both bare Al and $BiF_3@Al$ show four peaks at 284.8, 285.9, 287.5, and 289.5 eV, corresponding to C-C, C-O-C, O-C=O, and C=O, respectively. Peaks at 532.0 and 534.2 eV attribute to C-O and RO-COONa, both derived from diglyme decomposition. Notably, $BiF_3@Al$ exhibits lower O-C=O and RO-COONa contents compared to bare Al, with a faster C content decrease as etching depth increases, indicating that the NaF formation suppresses diglyme reduction. In the F 1s spectra, peaks at 684.5 eV and 688.2 eV are ascribed to Na-F and P-F, respectively. While P-F arises from $NaPF_6$ decomposition, the higher Na-F content on $BiF_3@Al$ confirms in-situ NaF formation. Similarly, in the Na 1s spectra, peaks at 1071.3 and 1072.6 eV correspond to Na-O and Na-F, with NaF content significantly higher on $BiF_3@Al$ (15.9%) than bare Al (8.0%). As the etching depth increases, the proportion of NaF on $BiF_3@Al$ increases to 28.3%, and in contrast, it slightly decreases to 7.5% on bare Al. The atomic ratio of all elements on bare Al and $BiF_3@Al$ is shown in Supplementary Tables 1 and 2. It can be confidently stated that the introduction of BiF_3 increases the proportion of inorganic components in the interphase and thereby enhancing its mechanical properties, as the atomic ratio of C and O element decreases and the ratio of F and Na increases owing to the suppression of the decomposition of the organic solvent.

High resolution transmission electron microscope (HR-TEM) and selected area electron diffraction (SAED) further confirm the conversion of BiF_3 to Na_3Bi and NaF. In Supplementary Fig. 10a, the lattice fringes measuring 0.333 and 0.231 nm correspond to the (102) plane of Na_3Bi and the (002) plane of NaF, respectively. SAED patterns also corroborates the presence of Na_3Bi and NaF (Supplementary Fig. 10b), specifically displaying the (102) and (203) planes of Na_3Bi and the (002) plane of NaF. Similar results are observed in X-ray diffraction (XRD) patterns of discharged BiF_3 (Supplementary Fig. 11), as it exhibits peaks that corresponds to the standard peaks of Na_3Bi (JCPDS No. 04-0351) and NaF (JCPDS No. 36-1455) as well as the standard peaks of Bi (JCPDS No. 44-1216). These results provide evidence that BiF_3 introduces an NaF-rich and sodiophilic Bi-contained interphase expectedly.

To confirm the effectiveness of NaF on boosting the SEI property, Na^+ diffusion barriers through NaF and Na_2O , the two primary SEI inorganic components, were investigated via DFT calculation. As shown in Supplementary Fig. 12 and Supplementary Data 1, NaF exhibits a lower Na^+ diffusion barrier (0.022 eV) than Na_2O (0.031 eV), indicating fast Na^+ transport kinetics in the NaF-rich interphase, which also confirms that the in-situ formation of NaF is beneficial to the fast-

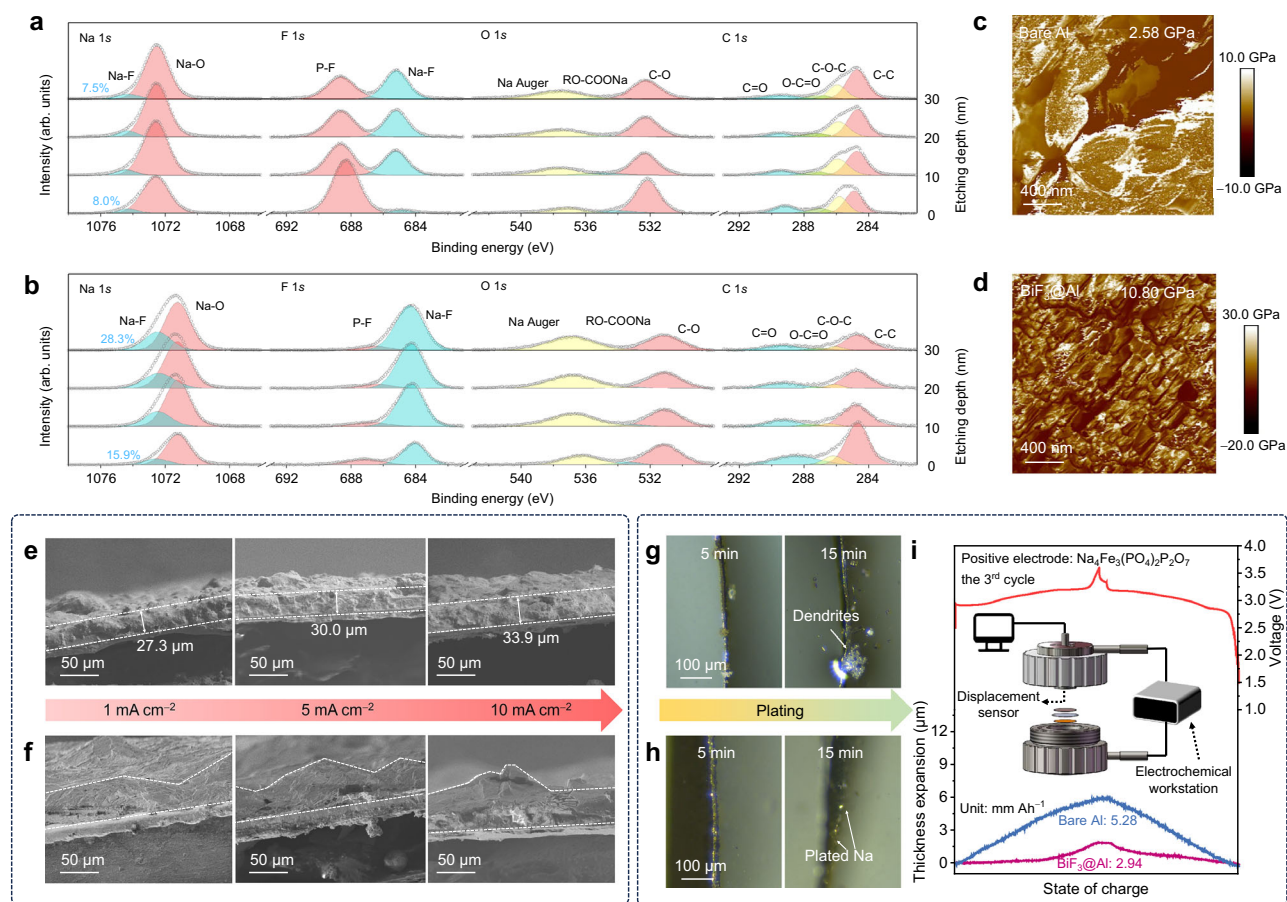


Fig. 3 | SEI properties and Na growth behaviors on bare Al and BiF₃@Al. XPS depth profiles of bare Al (a) and BiF₃@Al (b) after 20 cycles of Na plating/stripping at 25 °C and 10 mA cm⁻²@1 mAh cm⁻². Young's modulus maps of bare Al (c) and BiF₃@Al (d) after 20 cycles of Na plating/stripping at 25 °C and 10 mA cm⁻²@1 mAh cm⁻². Cross-section SEM images of 1 mA cm⁻² of Na plated on

bare Al (e) and BiF₃@Al (f) at 1, 5, and 10 mA cm⁻² at 25 °C. In-situ optical microscopy of Na plated on bare Al (g) and BiF₃@Al (h) at 1 mA cm⁻² at 25 °C. i Voltage profile and the in-situ thickness expansion curves of Al||Na₄Fe₃(PO₄)₂P₂O₇ and BiF₃@Al||Na₄Fe₃(PO₄)₂P₂O₇ anode-free sodium batteries at 25 °C. Inset: Schematic illustration of the in-situ thickness monitoring system.

charge performance. It is worth mentioning that the pure Bi-derived interphase (corresponding modified current collector is named as Bi@Al) shows similar overpotential as the BiF₃-derived interphase, but Bi@Al exhibits a lower average CE of 99.59% than that of BiF₃@Al (99.85%) in the 2nd–100th cycles, and its performance under harsh condition become worse (Supplementary Fig. 13). Top-view SEM of plated Na on Bi@Al (Supplementary Fig. 14) revealed that although uniform morphology can be observed at 1 mA cm⁻²@1 mAh cm⁻², the plated Na under high current density (10 mA cm⁻²@1 mAh cm⁻²) shows a locally even morphology with obvious cracks and holes. These phenomena indicate the essentiality of in-situ introduction of NaF in the interphase. Furthermore, atomic force microscope (AFM) was applied to understand the mechanical properties of SEI on the surface of bare Al and BiF₃@Al. Figure 3c, d show the Young's modulus maps of bare Al and BiF₃@Al after 20 cycles of Na plating/stripping at 10 mA cm⁻²@1 mAh cm⁻², respectively. The BiF₃@Al exhibits a higher Young's modulus of 10.80 GPa than bare Al (2.58 GPa). Moreover, in Supplementary Fig. 15, the cycled BiF₃@Al shows a flatter surface with a lower root mean square height (R_q , 39.3 nm) compared with that of bare Al (86.3 nm). In addition, Bi@Al shows middle value (8.74 GPa and 63.6 nm, Supplementary Fig. 16), indicating the synergy between bismuth and fluorine in promoting interphase properties. All results suggest that the formation of NaF enhances the mechanical properties of the SEI and the Na⁺ transfer kinetics and suppresses Na dendrite growth, contributing to stable Na plating/stripping at high current density.

SEM analysis of Na deposition morphology further highlights the advantages of BiF₃, as shown in Supplementary Fig. 17. At 1 mA cm⁻²@1 mAh cm⁻², bare Al exhibits a porous surface with needle-like features. As the areal capacity increases to 5 mAh cm⁻², cracks appear on deposited Na, which might be caused by the collapse and reconstruction of SEI during plating process (Supplementary Fig. 17c). The morphology even worsens at higher current densities (10 mA cm⁻²@5 mAh cm⁻², Supplementary Fig. 17e), as more cracks and holes are observed on the surface of deposited Na. In contrast, BiF₃@Al shows smooth and even Na deposition under identical conditions (Supplementary Fig. 17b, d) and still maintains uniform spherical protrusions even at the harsh condition of 10 mA cm⁻²@5 mAh cm⁻² (Supplementary Fig. 17f). Cross-section SEM images of 1 mA cm⁻² of Na plating on bare Al and BiF₃@Al at different current densities show that the plated Na on BiF₃@Al is dense and uniform with minor thickness change (27.3–33.9 μm) as the current densities increase from 1 to 10 mA cm⁻² (Fig. 3e). In contrast, Na plated on bare Al exhibits a loose and porous morphology with uneven distribution at both low and high current densities (Fig. 3f). As shown in Supplementary Fig. 18, the plated Na exhibits uniform distribution at various current densities by energy dispersive spectroscopy (EDS) mapping, while relatively weak Na signals can be captured on bare Al. Na plating morphology at both high current density and high areal capacity (10 mA cm⁻²@5 mAh cm⁻²) further reveal denser Na layers on BiF₃@Al compared to bare Al, with respective thicknesses of 99 and

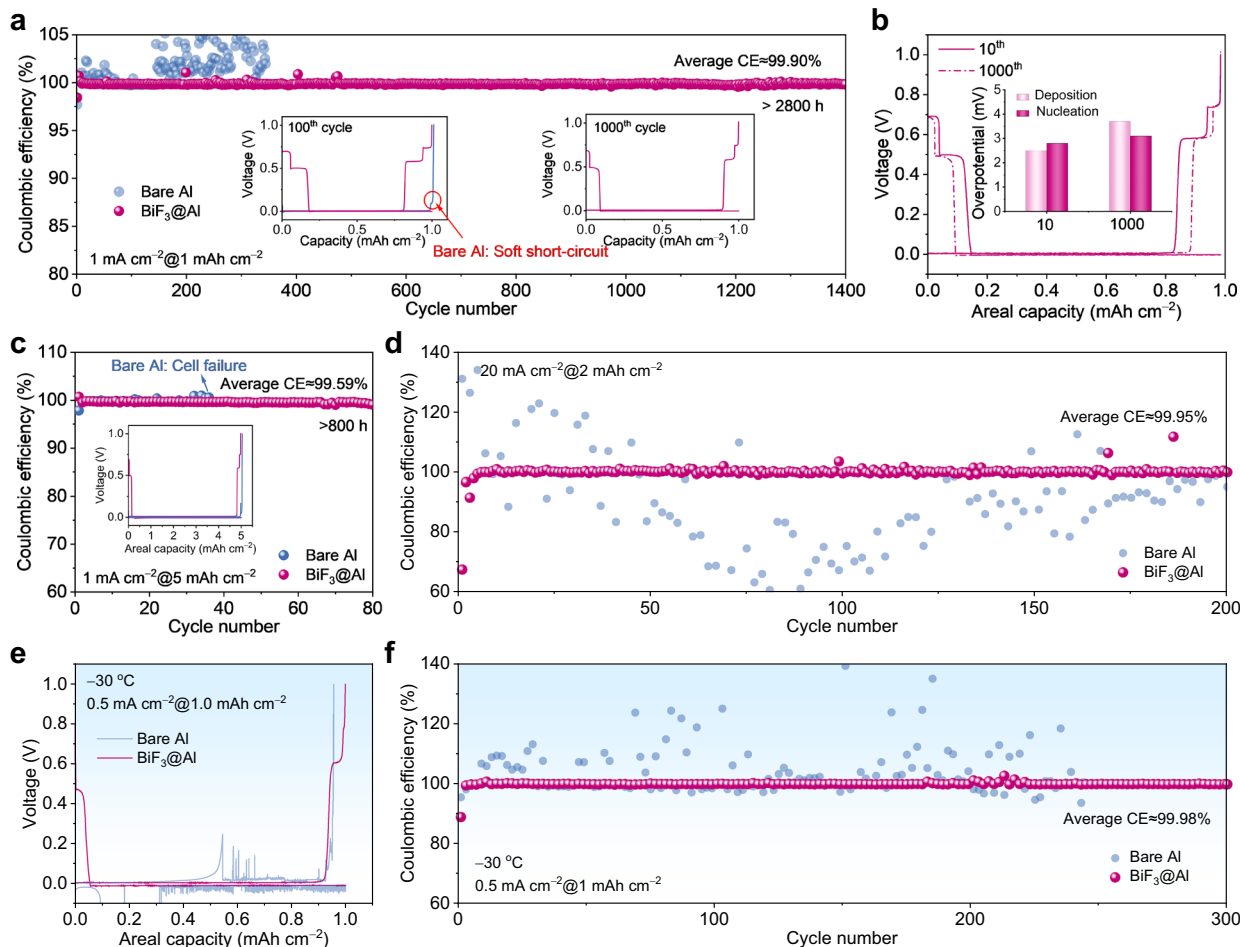


Fig. 4 | Reversible Na plating/stripping behavior on bare Al and $\text{BiF}_3@\text{Al}$. **a** CEs of Na plating/stripping of $\text{Na}||\text{Al}$ and $\text{Na}||\text{BiF}_3@\text{Al}$ cells at $1 \text{ mA cm}^{-2}@1 \text{ mAh cm}^{-2}$ at 25°C . Inset: voltage profiles of $\text{Na}||\text{Al}$ and $\text{Na}||\text{BiF}_3@\text{Al}$ cells at the 100th and 1000th cycles. **b** Voltage profiles of $\text{Na}||\text{BiF}_3@\text{Al}$ cells at the 10th and 1000th cycle at 25°C . Inset: corresponding nucleation and deposition overpotential. **c** CEs of Na

plating/stripping of $\text{Na}||\text{Al}$ and $\text{Na}||\text{BiF}_3@\text{Al}$ cells at $1 \text{ mA cm}^{-2}@5 \text{ mAh cm}^{-2}$ at 25°C . Inset: voltage profiles of the 10th cycle. **d** CEs of Na plating/stripping of $\text{Na}||\text{Al}$ and $\text{Na}||\text{BiF}_3@\text{Al}$ cells at $20 \text{ mA cm}^{-2}@2 \text{ mAh cm}^{-2}$ at 25°C . **e** Voltage profiles of $\text{Na}||\text{Al}$ and $\text{Na}||\text{BiF}_3@\text{Al}$ cells at -30°C and $0.5 \text{ mA cm}^{-2}@1 \text{ mAh cm}^{-2}$. **f** CEs of Na plating/stripping of $\text{Na}||\text{Al}$ and $\text{Na}||\text{BiF}_3@\text{Al}$ cells at -30°C and $0.5 \text{ mA cm}^{-2}@1 \text{ mAh cm}^{-2}$.

$168 \mu\text{m}$ (Supplementary Fig. 19). These demonstrate the role of BiF_3 in suppressing dendrite and mitigating volume expansion during cycling.

In order to further visualize the function of BiF_3 -derived interphase in suppressing Na dendrite growth and volume expansion, in-situ measurements were introduced, including in-situ optical microscopy and in-situ thickness tests. The in-situ optical microscopy of Na plating on bare Al and $\text{BiF}_3@\text{Al}$ was conducted, as shown in Fig. 3g, h. Na plated on bare Al exhibits a dendritic morphology with detachment, while $\text{BiF}_3@\text{Al}$ demonstrates uniform Na plating. In-situ thickness tests directly confirm that BiF_3 -derived interphase reduces volume expansion during Na deposition on the negative electrode side. Specifically, paired with a $\text{Na}_4\text{Fe}_3(\text{PO}_4)_2\text{P}_2\text{O}_7$ (NFPP) positive electrode to form an AFSB, $\text{BiF}_3@\text{Al}$ displays decreased thickness change per unit capacity (2.94 mm Ah^{-1}) compared to bare Al (5.28 mm Ah^{-1}) (Fig. 3i). These findings collectively demonstrate the efficacy of BiF_3 -derived interphase for AFSBs, particularly under harsh conditions.

Na plating and Na stripping are two independent processes corresponding to battery charging and discharging. To evaluate the role of BiF_3 -derived interphase in regulating Na stripping behavior, morphology of partially stripped and fully stripped Al and $\text{BiF}_3@\text{Al}$ was investigated, as shown in Supplementary Fig. 20. The charging and discharging current densities were both set as 10 mA cm^{-2} . After 6 min of charging, theoretically 1 mAh cm^{-2} of Na was plated on both current

collector with needle-like and uniform morphology, respectively (Supplementary Fig. 20a, b), and similar morphology can be observed on each of them after 3 min of discharging (Supplementary Fig. 20c, d). After charging to 1 V, a large amount of residual Na can be observed on bare Al (Supplementary Fig. 20e, g), while no residual Na can be observed on $\text{BiF}_3@\text{Al}$. (Supplementary Fig. 20f, h). Furthermore, the morphology of $\text{BiF}_3@\text{Al}$ current collector after sodiation and cycling at high current densities was shown in Supplementary Fig. 21. The sodiation product of BiF_3 evenly distribute on the current collector, and its morphology sustains stable after 50 cycles under a high current density of 10 mA cm^{-2} . These phenomena, together with the stable CEs of $\text{BiF}_3@\text{Al}$, prove the regulation effect of BiF_3 -derived interphase on Na stripping and its structure stability.

Reversible plating/stripping of Na on $\text{BiF}_3@\text{Al}$ under different conditions

To explore the important role of BiF_3 in regulating reversible Na plating/stripping, $\text{Na}||\text{BiF}_3@\text{Al}$ and $\text{Na}||\text{Al}$ cells were assembled using 1.0 M NaPF_6 -diglyme electrolyte. In Fig. 4a, $\text{BiF}_3@\text{Al}$ shows extended cycle stability with an average CE of $\sim 99.90\%$ over 1400 cycles at $1 \text{ mA cm}^{-2}@1 \text{ mAh cm}^{-2}$. In contrast, bare Al displays severe CE fluctuations and fails only after 330 cycles. Furthermore, bare Al suffers from soft short-circuit during Na stripping after 100 cycles, while the voltage profiles of $\text{BiF}_3@\text{Al}$ remain stable even after 1000 cycles, as

shown in insets of Fig. 4a. In Fig. 4b and Supplementary Fig. 22, BiF₃@Al still maintains low nucleation and deposition overpotentials of 2–4 mV during cycling. In contrast, although bare Al also shows a low deposition overpotential of ~2 mV during the 300 cycles, it shows higher nucleation overpotentials of 15–25 mV, indicating the role of BiF₃-derived interphase in enhancing Na nucleation kinetics.

Increased plating areal capacity, higher current densities, and lowering ambient temperature generally elevate the risk of dendrite formation and side reactions, leading to a lower CE. Figure 4c–f shows the CE of BiF₃@Al under different harsh test conditions. In Fig. 4c, at a higher areal capacity of 5 mAh cm⁻², BiF₃@Al also demonstrates improved stability with an average CE of 99.59% over 800 h, whereas bare Al shows a much shorter cycle life of only 400 h with severe soft short-circuit during cycling. This result further underscores the role of BiF₃ in promoting uniform Na plating and growth at high capacity. Supplementary Figs. 23 and 4d show the rate capabilities of BiF₃ at different high current densities. BiF₃@Al performs stable CE of 99.80% and 99.81% at 2 mA cm⁻²@2 mAh cm⁻² and 10 mA cm⁻²@1 mAh cm⁻², respectively, whereas bare Al experiences significant CE fluctuations. Even at an extreme condition of 20 mA cm⁻²@2 mAh cm⁻², BiF₃@Al still maintains stable for over 200 cycles with an average CE of 99.95%. These results further validate the crucial role of the BiF₃-derived sodiophilic interphase in achieving fast kinetics in AFSBs. Compared with previously reported works on sodium metal batteries (SMBs) and AFSBs, BiF₃@Al demonstrates high maximum current density, enhanced areal capacity and extended cycle life at room temperature (Supplementary Fig. 24).

The CE of Na plating/stripping under low-temperature (–30 °C) was also investigated. In Supplementary Fig. 25, BiF₃@Al not only dramatically reduces the nucleation overpotential (3.6 mV compared to 36.2 mV for bare Al) but also slightly reduced the deposition overpotential (7.1 mV compared to 8.8 mV for bare Al), suggesting improved kinetics enabled by BiF₃-derived interphase under low-temperature conditions. Thanks to the lower nucleation and deposition overpotentials on BiF₃@Al, it maintains stability with a high average CE of ~99.98% over 300 cycles at 0.5 mA cm⁻²@1 mAh cm⁻², as shown Fig. 4f, g. In contrast, under the same conditions, bare Al suffers from severe soft short circuits. Additionally, BiF₃@Al still maintains stability at higher current densities of 1 mA cm⁻² and 1.5 mA cm⁻² with an areal capacity of 1 mAh cm⁻² (Supplementary Fig. 26). The plated Na on BiF₃@Al under low-temperature exhibits smooth morphology (Supplementary Fig. 27), indicating that the Na plating kinetics is still promoted under low-temperature. As the 1.0 M NaPF₆-diglyme electrolyte freezes under –40 °C, we prepared an optimized electrolyte (0.5 M NaPF₆ in diglyme/1,3-dioxolane, 1:1 in volume), which remains liquid under such low temperature (Supplementary Fig. 28). Using this electrolyte, Na||BiF₃@Al achieves stable operation under –40 °C (Supplementary Fig. 29), indicating the universality of our fluorinated sodiophilic interphase strategy. These results implies that BiF₃@Al has the potential to operate at high current density under low temperatures.

Performance of high-power and low-temperature BiF₃@Al||Na₄Fe₃(PO₄)₂P₂O₇ AFSBs

To validate the above effects of BiF₃-derived interphase, initially anode-free sodium batteries were assembled by integrating BiF₃@Al with NFPP positive electrode (named BiF₃@Al||NFPP). For comparison, Al||NFPP AFSBs were assembled. As expected, the BiF₃@Al||NFPP AFSB exhibits better rate performance compared to Al||NFPP. In Fig. 5a, BiF₃@Al||NFPP with a high positive electrode mass loading of ~10 mg cm⁻² exhibits a high initial specific capacity of 98.7 mAh g⁻¹ at 0.2 C. Reversible specific capacities of 84.6, 79.8, 74.3, 69.8, 64.9, and 57.4 mAh g⁻¹ are achieved at 0.5, 1, 2, 5, 10, and 20 C, respectively, indicating a good rate capability of BiF₃@Al||NFPP AFSB. In contrast, Al||NFPP only shows a low specific capacity

of 81.5 mAh g⁻¹ at 0.2 C, and rapidly fades to 65.6 mAh g⁻¹ in only 5 cycles. The poor Na plating/stripping kinetics and reversibility of Al worsens the performance of Al||NFPP at rates higher than 0.5 C, as it suffers from severe capacity fluctuations and fails after 70 cycles. Voltage profiles at different rates (Fig. 5b) show that the BiF₃@Al||NFPP cell remains stable charge plateau and low polarization at high rates.

In terms of cycle performance, BiF₃@Al||NFPP exhibits high cycle stability at 1C (~75 mAh g⁻¹, over 400 cycles) and 5C (~65 mAh g⁻¹, over 200 cycles, Supplementary Fig. 30). Furthermore, BiF₃@Al||NFPP maintains a capacity retention of 75.9% after 300 cycles at 10 C (Fig. 5c), where the areal current density is up to 10 mA cm⁻². Even with a higher positive electrode mass loading of 22 mg cm⁻², BiF₃@Al||NFPP AFSB still remains stable for over 160 cycles at 0.5 C charge and 1.0 C discharge rate with a capacity retention of ~70.7% (Fig. 5d). Compared to other reported Na-metal-based batteries, our BiF₃@Al||NFPP AFSB exhibits high operating rate (20C) without any pre-loaded Na metal (Fig. 5e), breaking the trade-off in power density and energy density of Na-based batteries^{3,5,6,13,18,19,22,32–38}.

Notably, the BiF₃@Al current collector is prepared by a tradition stirring-coating strategy with a decent amount of acetylene black (AB) additive in the BiF₃ slurry, which is a simple, low-cost and widely used strategy to prepare electrodes both in laboratory and practical production. In order to explore the influence of the addition of conductive carbon, pure AB and pure BiF₃ slurries were also prepared and coated onto Al current collector (Supplementary Fig. 31), named AB@Al and p-BiF₃@Al, respectively. The rate performance of Na plating on these two current collectors and corresponding full-cell performance was shown in Supplementary Fig. 32. AB@Al demonstrated average Coulombic efficiency of 99.80% and 99.05% at 1 mA cm⁻²@1 mAh cm⁻² and 5 mA cm⁻²@1 mAh cm⁻², respectively, lower than that of BiF₃@Al, especially at high current density, indicating the critical role of BiF₃ in regulating Na nucleation and plating kinetics. Additionally, Na||p-BiF₃@Al cells suffered from soft short-circuit at both 1 mA cm⁻²@1 mAh cm⁻² and 5 mA cm⁻²@1 mAh cm⁻², indicating the importance of acetylene black in the electrode to promote the conductivity. Furthermore, p-BiF₃@Al||NFPP full cells failed to be charged, while AB@Al||NFPP full cells suffered from severe capacity decay at 1C. These results demonstrate that the AB additive is essential in BiF₃@Al. The mass loading of BiF₃ on Al is controlled at around 0.2 mg cm⁻², as excessive BiF₃ does not significantly reduce the overpotential, but may cause active Na loss, which is not conducive to the cycle performance (Supplementary Fig. 33).

To demonstrate the practicability of BiF₃@Al||NFPP AFSB, its electrochemical performance at low temperatures was investigated. BiF₃@Al||NFPP exhibits the ability of operating at –30 °C at high rates (above 1 C). In Fig. 5f and Supplementary Fig. 34, BiF₃@Al||NFPP shows capacity retentions of 87.0%, 76.6%, 62.4% and 50.0% at 0.6, 1.0, 1.5 and 2.0 C at –30 °C (vs. 66.2 mAh g⁻¹ at 0.2 C). As a consequence of plating/stripping reversibility under low temperature condition, BiF₃@Al||NFPP shows prolonged cyclability at –30 °C (over 1600 cycles with minimal capacity decay, Fig. 5g and Supplementary Fig. 35). The cycle stability and average CE under low-temperature is even higher than that under room-temperature, which is because the side reaction of electrolyte on both negative and positive electrode sides are suppressed under cryogenic condition. (Supplementary Fig. 36). Using the optimized electrolyte, BiF₃@Al||NFPP achieves stable cycling for 240 cycles with 92.3% capacity retention at a high rate of 1C (Supplementary Fig. 37), which reflects the potential of our BiF₃@Al||NFPP AFSB to operate at extremely low temperatures. The Ragone plots (Supplementary Fig. 38) reveal that BiF₃@Al||NFPP not only achieves high specific energies of 284.7 Wh kg⁻¹ at 25 °C and 200.8 Wh kg⁻¹ at –30 °C (based on the total mass of active materials on negative and positive electrode), but also delivers high specific powers of 8257.5 W kg⁻¹ at 25 °C (with a specific energy of 112.4 Wh kg⁻¹) and

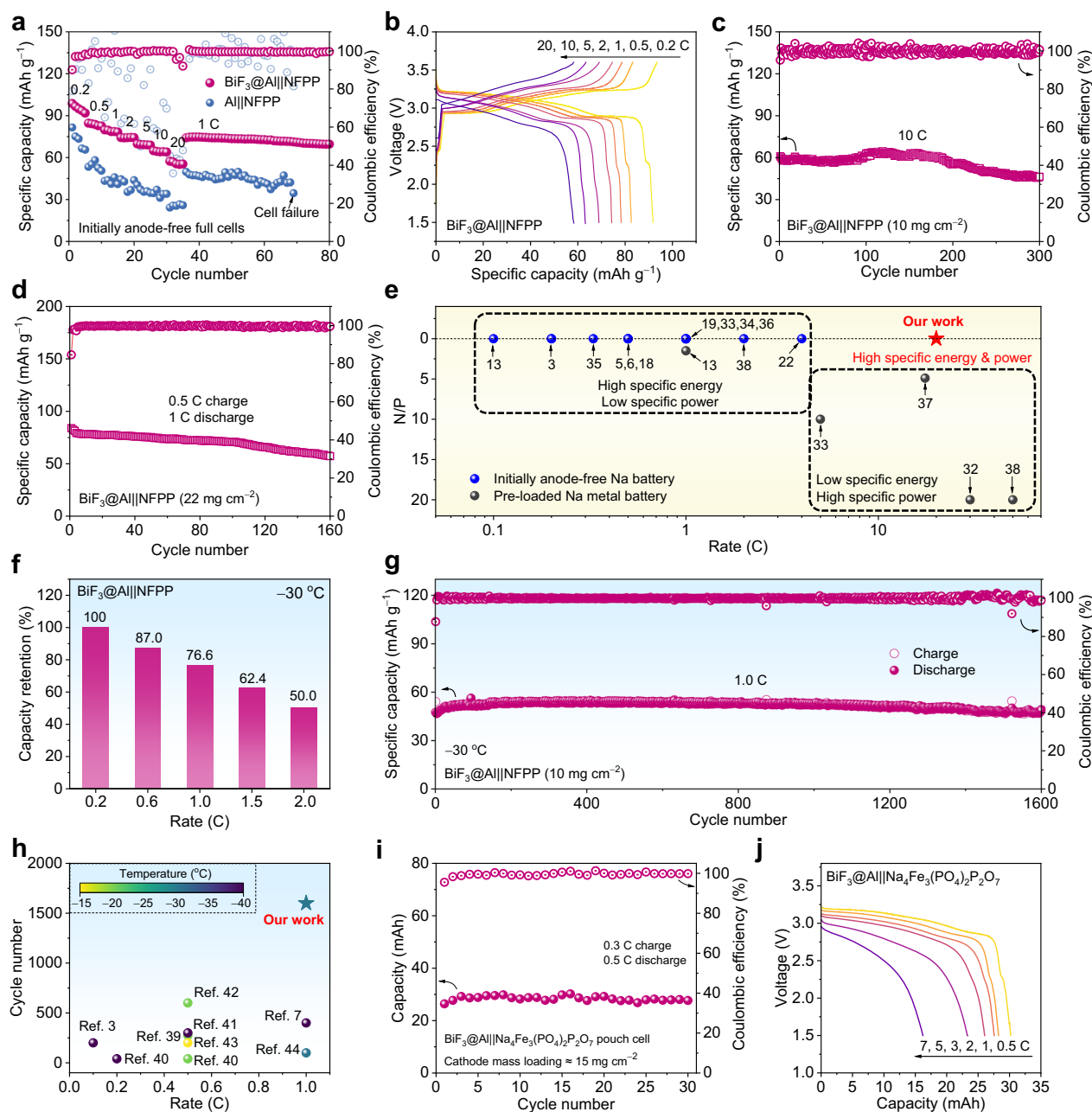


Fig. 5 | Electrochemical performance of BiF₃@Al||Na₄Fe₃(PO₄)₂P₂O₇ initially anode-free sodium batteries. **a** Rate performance of Al||NFPP and BiF₃@Al||NFPP anode-free sodium batteries at 25 °C. **b** Voltage profiles of BiF₃@Al||NFPP from 0.2 to 20 C at 25 °C. **c** Cycle performance of BiF₃@Al||NFPP at 10 C at 25 °C. **d** Cycle performance of BiF₃@Al||NFPP at 0.5 C charge and 1.0 C discharge with positive electrode mass loading of 22 mg cm⁻² at 25 °C. **e** Comparisons of N/P ratio and operating rate of our work with other reported Na-metal-based batteries. **f** Capacity

retention of BiF₃@Al||NFPP from 0.2 to 2.0 C rate at -30 °C. **g** Cycle performance of BiF₃@Al||NFPP AFSBs at 1.0 C under -30 °C. **h** Comparison of rate and cycle number of our work with other reported low-temperature SMBs and AFSBs. **i** Cycle performance of BiF₃@Al||NFPP anode-free pouch cell at 0.3 C charge and 0.5 C discharge at 25 °C. **j** Voltage profiles of BiF₃@Al||NFPP anode-free pouch cell at various discharging rates at 25 °C. Note: 1 C = 100 mA g⁻¹.

486.9 W kg⁻¹ (80.7 Wh kg⁻¹) at -30 °C. Our BiF₃@Al||NFPP full batteries show comparable rate performance and cyclability with other published low-temperature SMBs and AFSBs (Fig. 5h and Supplementary Table 3)^{3,7,39–44}.

To explore the potential of BiF₃ for AFSBs with higher energy density, we fabricated initially anode-free batteries with a layered oxide NaNi_{1/3}Fe_{1/3}Mn_{1/3}O₂ (NFM) positive electrode. The BiF₃@Al||NFM AFSB exhibits a higher energy density of 331.0 Wh kg⁻¹ (based on the total mass of active materials on negative and positive electrode) and

remains stable at 2 C (Supplementary Fig. 39), which points out the potential of BiF₃ to be applied in energy-denser AFSBs with optimized positive electrodes and electrolytes. To further demonstrate the practical viability of BiF₃, 30 mAh initially anode-free pouch-cells were assembled with a high positive electrode mass loading of -15 mg cm⁻². In Fig. 5i, j, the pouch cells remain stable and demonstrate rate discharge capabilities of 30.1, 28.3, 27.6, 26.1, 23.3, and 16.2 mAh at 0.5, 1, 2, 3, 5, and 7 C, respectively. These results indicate BiF₃ has a promising prospect for commercial applications.

Discussion

In summary, we proposed a fluoride sodiophilic interphase design strategy towards high-power initially anode-free sodium battery. Through a systematic comparison of the chemical, crystallographic, and electrochemical properties of six metal fluorides, BiF₃ emerged as the optimal modifier owing to the highest sodiophilicity. SEM and FEA demonstrated uniform Na nucleation on BiF₃@Al at high current density. By XPS depth profiling, HR-TEM, XRD, AFM, and theoretical calculation, we confirmed the in-situ formation of NaF and its role in mitigating volume expansion and regulating Na growth process. Consequently, Na||BiF₃@Al exhibited an extended cycle life (>2800 h) and high-rate capability (20 mA cm⁻²), as well as low-temperature adaptability (an average CE of 99.98% at -30 °C). The BiF₃@Al||NFPP full battery not only achieves high specific energies (284.7 Wh kg⁻¹ at 25 °C and 200.8 Wh kg⁻¹ at -30 °C) and specific powers (8257.5 W kg⁻¹ at 25 °C and 486.9 W kg⁻¹ at -30 °C), but also demonstrates prolonged cycle performance (over 1600 cycles) at -30 °C. BiF₃@Al||NFPP pouch cells can operate at a high rate of 7 C with practical-level mass loading of positive electrode, underscoring their commercial potential. This work provides insights to perform stable AFSBs at high-rate and low-temperature, advancing its commercialization process.

Methods

Materials

Na cubes (≥99.9%) stored in mineral oil were purchased from Sino-pharm Chemical Reagent Co., Ltd. (China). Sodium hexafluorophosphate (NaPF₆, 99.9%) and polyvinylidene difluoride (PVDF, M.W. >1,000,000) were purchased from Suzhou Duo Duo Co., Ltd. (China). Bismuth (III) fluoride (BiF₃, 99%) and Zinc (II) fluoride (ZnF₂, 99%) were purchased from Aladdin Co., Ltd. (China). Iron (III) fluoride (FeF₃, 97% min), Cobalt (II) fluoride (CoF₂, 99%), Nickel (II) fluoride (97%), Tin (II) fluoride (SnF₂, 99%) and Diethylene glycol dimethyl ether (diglyme anhydrous, 99.5+%) were purchased from Thermo Fisher Scientific Co., Ltd. (America). The carbonate electrolyte (1.0 M NaClO₄ in EC/DEC, 1:1 in volume, with 5 vol.% FEC additive) was purchased from Suzhou Duo Duo Co., Ltd. (China). Bismuth powder (99.99% metals basis, 325 meshes) was purchased from TCI (Shanghai) development Co., Ltd. (China). Positive electrode materials (Na₄Fe₃(PO₄)₂P₂O₇ and NaNi_{1/3}Fe_{1/3}Mn_{1/3}O₂) were purchased from Hefei Kejing Co., Ltd. Acetylene black (AB, Denka Black Li-2060) was purchased from SaiBo Electrochemical Material Co., Ltd. (China). N-methyl pyrrolidinone (NMP, 99.9%, electronic grade) and 1,3-dioxolane (DOL, 99.5+%, extra dry) were purchased from Sigma-Aldrich (America). The aluminum foils (Thickness: 12 μm), carbon coated aluminum foils (Thickness: 12 μm; carbon mass loading: 0.05 mg cm⁻²) and Celgard 2325 separator (PP/PE/PP separator, thickness: 25 μm; Gurley value: 620 s; porosity: 40%; average pore size: 0.03 μm) were purchased from Nanjing Mojiesi Energy Technology Co., Ltd. (China).

Preparation of electrodes and electrolytes

The slurries for negative electrode current collector were prepared by mixing active materials (FeF₃, CoF₂, NiF₂, SnF₂, ZnF₂ and BiF₃), Acetylene black, PVDF in a ratio of 8:1:1 by mass ratio in NMP solvent. The slurries were coated on an aluminum foil (Al) using a doctor blade, and then dried at 80 ± 0.1 °C for over 12 h in a vacuum oven before use. The positive electrode slurries were prepared by mixing active materials (Na₄Fe₃(PO₄)₂P₂O₇ and NaNi_{1/3}Fe_{1/3}Mn_{1/3}O₂), Acetylene black, PVDF in a ratio of 9:0.5:0.5 by mass ratio in NMP solvent. The slurries were coated on a carbon coated aluminum foil using a doctor blade and then dried at 120 ± 0.1 °C for over 12 h in a vacuum oven. All electrodes were rolled by a roller machine (Shenzhen Kejing Star Technology Co., Ltd., China) before use. The mass loading of the metal fluorides was around 0.2 mg cm⁻², and the mass loading of positive electrode material varied from -7 mg cm⁻² to -22 mg cm⁻². The negative and positive electrodes were cut into round pieces with diameters of

12 mm and 10 mm, respectively. The electrolyte was prepared by adding 1 mol L⁻¹ NaPF₆ into diglyme solvent in an argon filled glove box (MIKROUNA, China), where the contents of both O₂ and H₂O were below 0.01 ppm. The electrolyte was dried using 4 Å molecular sieves (Aladdin Co., Ltd., China) for 48 h before use. Na metal pieces with diameters of 8, 10, and 12 mm were cut from Na cubes and used immediately after cutting. All electrodes and electrolytes are stored in the glove box, where the environment temperature is 25 ± 1 °C.

Electrochemical measurements

Electrochemical properties were carried out by CR2032-type coin cells assembled in an argon filled glove box. Na||Al and Na||MF_x cells were assembled using the prepared positive electrode current collector and sodium pieces with a diameter of 8 mm, with 40 μL electrolytes and Celgard 2325 separators with a diameter of 16 mm. The thickness of sodium pieces is -100 μm. Coin-type full-cells were assembled using pre-cycled negative and positive electrodes with 40 μL electrolytes and Celgard 2325 separators with a diameter of 16 mm. The cells were placed in a constant temperature chamber (25 ± 0.2 °C) to obtain room-temperature performance. The batteries were placed in the DW-HL398 ultralow temperature freezer box (Zhongke Meiling Cryogenic Technology Co., Ltd.) to obtain low-temperature performance. Cycle performance of the assembled cells was carried out by a LAND battery test system (CT2001A). Linear sweep voltammetry was carried out by an EC-Lab chemical working station (Bio-Logic, France). The scan rate was set as 2 mV s⁻¹, and the cut-off voltage was set as -0.05 V and 4.5 V for anodic scan and cathodic scan, respectively. The single-layer BiF₃@Al||Na₄Fe₃(PO₄)₂P₂O₇ pouch cells were assembled by one piece of single-face coated BiF₃ (mass loading: -0.2 mg cm⁻²) on aluminum foil and one piece of single-face coated Na₄Fe₃(PO₄)₂P₂O₇ (mass loading: -15 mg cm⁻²) on carbon coated aluminum foil with an area of 4.5 × 5.8 cm and 4.3 × 5.6 cm, respectively. 0.4 mL of 1.0 M NaPF₆-diglyme electrolyte was injected before sealing. The pouch cells were pre-cycled at 0.1 °C for 2 cycles, and then removed the excessive gas under vacuum and then sealing again. The external pressure of the pouch cell during cycling is 0.5 MPa.

Characterization

X-ray diffraction was performed by D8AD VANCE with Cu Kα radiation at 40 kV and 20 mA. Scanning electron microscopy images were observed using an Ultra 55 microscope (Germany) operated at 3.0 kV. High-resolution transmission electron microscopy (HR-TEM) images were observed by a Talos F200X (FEI) microscope (USA) operated at 200 kV. XPS depth profile was investigated using an X-ray photoelectron spectrometer (Thermo Kalpha). Atomic force microscope (AFM) tests were performed using Bruker Dimension Icon. In-situ thickness tests were carried out by RSS1400 (Initial Energy Science & Technology Co., Ltd., China). All electrodes used for ex-situ characterization were obtained by disassembling Na||MF_x@Al cells in the glove box, where the environment temperature is 25 ± 1 °C.

Theoretical calculation

Theoretical calculations were performed by Vienna ab initio simulation package (VASP)^{45,46} code. To describe the exchange-correlation energy, the generalized gradient approximations (GGA) of Perdew–Burke–Ernzerhof (PBE)⁴⁷ pseudopotentials were applied in our calculations. A vacuum space of 20 Å was used in the z-axis direction to avoid the interaction. The energy cutoff of 510 eV was applied in our calculations. The climbing-image nudged elastic band method (CI-NEB)⁴⁸ is applied for computing decomposition barriers.

Governing equations

The simulation was performed using the COMSOL 6.3 Multiphysics simulation software. The deposition process on four different substrate surfaces was considered in the simulation, with the substrates

being Na₃Bi, NaZn₁₃, Co, and Al. In terms of modeling, the simulation first constructed an 8 × 9 μm computational domain, which was then divided into two regions: the electrolyte and the substrate. The substrate thickness was uniformly set to 1 μm (this does not represent the actual thickness of the substrate but rather only accounts for the substrate surface). The following is a description of the theoretical methods used in the simulation, including theoretical equations and corresponding explanations^{49–51}:

$$\frac{\partial c_i}{\partial t} + \nabla \cdot J_i = R_i \quad (3)$$

$$J_i = -D_i \nabla c_i - z_i u_i F c_i \nabla \phi_i \quad (4)$$

$$\sum_i z_i c_i = 0 \quad (5)$$

$$\nabla \cdot i = F \sum_i z_i R_i \quad (6)$$

where c_i denotes the concentration, J_i is the mass flux for each species, $R_i = -\frac{v_i i_{loc}}{z_i F}$ is the electrochemical reaction source term, D_i is the diffusion coefficient, u_i is the mobility, z_i is the charge number, $i_i = \sum_m i_{loc,m}$ is the current density of electrolyte (m indicates the charge transfer electrode reaction), ϕ_i is the electrolyte potential, v_i is the stoichiometric coefficient, i_{loc} is the local current density at the electrode surface, and F is the Faraday constant. By coupling the above system of equations, the distribution of electric field and current density on the substrate surface and in the electrolyte region can be obtained.

Data availability

Source data are provided in the Source Data file with this paper. Source data are provided with this paper.

References

- Babu, B., Simon, P. & Balducci, A. Fast charging materials for high power applications. *Adv. Energy Mater.* **10**, 2001128 (2020).
- Heenan, T. M. M. et al. Mapping internal temperatures during high-rate battery applications. *Nature* **617**, 507–512 (2023).
- Zhu, Q. et al. H. A 110 Wh kg⁻¹ Ah-level anode-free sodium battery at -40 °C. *Joule* **8**, 1–14 (2024).
- Hu, Z. et al. Current progress of anode-free rechargeable sodium metal batteries: origin, challenges, strategies, and perspectives. *Adv. Funct. Mater.* **34**, 2313823 (2024).
- Dahunsi, O. J. et al. Anode-free Na metal batteries developed by nearly fully reversible Na plating on the Zn surface. *Nanoscale* **15**, 3255 (2023).
- Geng, M. et al. A stable anode-free Na–S full cell at room temperature. *Energy Storage Mater.* **52**, 230–237 (2022).
- Hu, L. et al. Restructuring electrolyte solvation by a versatile diluent toward beyond 99.9% coulombic efficiency of sodium plating/stripping at ultralow temperatures. *Adv. Mater.* **35**, 2312161 (2024).
- Assegie, A. A. et al. Multilayer-graphene-stabilized lithium deposition for anode-free lithium-metal batteries. *Nanoscale* **11**, 2710 (2019).
- Chen, W. et al. Laser-induced silicon oxide for anode-free lithium metal batteries. *Adv. Mater.* **32**, 2002850 (2020).
- Shan, C. et al. Cu-CNTs current collector fabricated by deformation-driven metallurgy for anode-free Li metal batteries. *Carbon* **204**, 367–376 (2023).
- Wu, Z. et al. Growing single-crystalline seeds on lithiophobic substrates to enable fast-charging lithium-metal batteries. *Nat. Energy* **8**, 340–350 (2023).
- Tao, J. et al. Advancing anode-less lithium metal batteries: ZnF₂ modification and in-situ structural regulation for enhanced performance. *J. Mater. Chem. A* **12**, 18127–18136 (2024).
- Ge, J. et al. Edge electron effect induced high-entropy SEI for durable anode-free sodium batteries. *Adv. Mater. Early View* **37**, 2413253 (2024).
- Lu, X. et al. From lab to application: challenges and opportunities in achieving fast charging with polyanionic cathodes for sodium-ion batteries. *Adv. Mater.* **36**, 2407359 (2024).
- Lin, K. et al. In situ constructed ionic-electronic dual-conducting scaffold with reinforced interface for high-performance sodium metal anodes. *Small* **17**, 2104021 (2021).
- Wang, H. et al. 3D Ag@C cloth for stable anode free sodium metal batteries. *Small Methods* **5**, 2001050 (2021).
- Lee, K. et al. A 3D hierarchical host with enhanced sodiophilicity enabling anode-free sodium-metal batteries. *Adv. Mater.* **34**, 2109767 (2022).
- Wang, C. et al. Robust anode-free sodium metal batteries enabled by artificial sodium formate interface. *Adv. Funct. Mater.* **13**, 2204125 (2023).
- Cheng, X. et al. In-situ alloy-modified sodiophilic current collectors for anode-less sodium metal batteries. *Batteries* **9**, 408 (2023).
- Huang, B. et al. Ultrahigh nitrogen content carbon nanosheets for high stable sodium metal anodes. *Adv. Sci.* **10**, 2206845 (2023).
- Wang, Y. et al. A high-power rechargeable sodium-ion full battery operating at -40 °C. *Adv. Funct. Mater.* **34**, 2315498 (2024).
- Xie, C. et al. Microalloying induced stable welded interfaces for highly reversible zero-excess sodium metal batteries. *Energy Environ. Sci.* **17**, 4228–4237 (2023).
- Zhao, Y. et al. An anode-free potassium-metal battery enabled by a directly grown graphene-modulated aluminum current collector. *Adv. Mater.* **34**, 2202902 (2022).
- Li, S. et al. Customized electrolyte and host structures enabling high-energy-density anode-free potassium-metal batteries. *ACS Energy Lett.* **8**, 3467–3475 (2023).
- Ren, N. et al. Design principles of mediation layer for current collectors toward high-performance anode-free potassium-metal batteries: a case study of Cu₆Sn₅ on copper. *Adv. Funct. Mater.* **34**, 2313538 (2024).
- Cui, Z. et al. Non-completely selenized Cu-OSe nanowires as potassium-philic host for anode-free potassium metal batteries. *Energy Storage Mater.* **71**, 103649 (2024).
- Bai, M. et al. An anodeless, mechanically flexible and energy/power dense sodium battery prototype. *Energy Environ. Sci.* **15**, 4686 (2022).
- Li, M. et al. Multifunctionalized safe separator toward practical sodium-metal batteries with high-performance under high mass loading. *Adv. Funct. Mater.* **33**, 2214759 (2023).
- Liu, H. et al. Multifunctional separator enables high-performance sodium metal batteries in carbonate-based electrolytes. *Adv. Mater.* **36**, 2307645 (2024).
- Zhang, Y.-Y. et al. Refined electrolyte and interfacial chemistry toward realization of high-energy anode-free rechargeable sodium batteries. *J. Am. Chem. Soc.* **145**, 25643–25652 (2023).
- Cui, C. et al. Unlocking the in situ Li plating dynamics and evolution mediated by diverse metallic substrates in all-solid-state batteries. *Sci. Adv.* **8**, eadd2000 (2022).
- Yu, Y. et al. Highly sodiophilic heterostructures toward dendrite-free sodium metal batteries. *Adv. Funct. Mater.* **34**, 2401914 (2024).
- Li, H. et al. Sodiophilic current collectors based on MOF-derived nanocomposites for anode-less Na-metal batteries. *Adv. Energy Mater.* **12**, 2202293 (2022).
- Liu, L. et al. Multifunctional high-entropy alloy nanolayer toward long-life anode-free sodium metal battery. *Adv. Mater.* **37**, 2413331 (2024).

35. Jiao, W. et al. Highly stable anode-free sodium batteries enabled by mechanically deformable nucleation interface. *Energy Storage Mater.* **73**, 103784 (2024).
36. Ruan, J. et al. Current collector interphase design for high-energy and stable anode-less sodium batteries. *Nat. Sustain.* **8**, 530–541 (2025).
37. Yuan, M. et al. Unlocking the ultrafast deposition kinetics within Bi-tailored core-shell structured carbon nanofibers for highly efficient and ultrastable sodium metal batteries. *Angew. Chem. Int. Ed.* **64**, e202417930 (2024).
38. Guo, W. et al. Outside-in directional sodium deposition through self-supporting gradient fluorinated magnesium alloy framework toward high-rate anode-free Na batteries. *Energy Storage Mater.* **73**, 103840 (2024).
39. Wang, Z. et al. Promoting fast Na ion transport at low temperatures for sodium metal batteries. *ACS Appl. Mater. Interfaces* **14**, 40985–40991 (2022).
40. Yu, D. et al. Low-temperature and fast-charge sodium metal batteries. *Small* **20**, 2311810 (2024).
41. Zhong, S. et al. Molecular engineering on solvation structure of carbonate electrolyte toward durable sodium metal battery at -40°C . *Angew. Chem. Int. Ed.* **62**, e202301169 (2023).
42. Zheng, X. et al. Knocking down the kinetic barriers towards fast-charging and low-temperature sodium metal batteries. *Energy Environ. Sci.* **14**, 4936 (2021).
43. Liu, R. et al. Exploring highly reversible 1.5-electron reactions ($\text{V}^{3+}/\text{V}^{4+}/\text{V}^{5+}$) in $\text{Na}_3\text{VCr}(\text{PO}_4)_3$ cathode for sodium-ion batteries. *ACS Appl. Mater. Interfaces* **9**, 43632–43639 (2017).
44. Wang, L. et al. Flexible self-supporting organic cathode with interface engineering for high-performance and wide-temperature sodium-ion batteries. *Carbon Energy* **6**, e632 (2024).
45. Kresse, G. & Furthmüller, J. Efficient iterative schemes for ab initio total-energy calculations using a plane-wave basis set. *Phys. Rev. B* **54**, 11169 (1996).
46. Kresse, G. & Joubert, D. From ultrasoft pseudopotentials to the projector augmented-wave method. *Phys. Rev. B* **59**, 1758 (1999).
47. Perdew, J. P., Burke, K. & Ernzerhof, M. Generalized gradient approximation made simple. *Phys. Rev. Lett.* **77**, 3865 (1996).
48. Henkelman, G., Uberuaga, B. P. & Jónsson, H. A climbing image nudged elastic band method for finding saddle points and minimum energy paths. *J. Chem. Phys.* **113**, 9901–9904 (2000).
49. Lee, S., Wang, W. & Chen, J. Diffusion-induced stresses in a hollow cylinder. *Mater. Sci. Eng. A* **285**, 186–194 (2000).
50. Xie, Z., Ma, Z., Wang, Y., Zhou, Y. & Lu, C. A kinetic model for diffusion and chemical reaction of silicon anode lithiation in lithium ion batteries. *RSC Adv.* **6**, 22383–22388 (2016).
51. Shen, X., Zhang, R., Shi, P., Chen, X. & Zhang, Q. How does external pressure shape Li dendrites in Li metal batteries? *Adv. Energy Mater.* **11**, 2003416 (2021).
- China (Nos. 52261135631, 52103335; Fei W.), the Science and Technology Commission of Shanghai Municipality (No. 23TS1401700; Fei W.).

Author contributions

M.W., J.R., and Fei W. conceived the idea for the project. M.W., J.Y., H.J., F.F., D.S., and Fei W. designed the experiments. M.W. and J.Y. assembled anode-free pouch cells. M.W., J.Y., H.J., Z.L., and Fengmei W. performed the characterization experiments. M.W., J.R. and Fei W. wrote the manuscript. All authors discussed the results and commented on the manuscript.

Competing interests

The authors declare no competing interests.

Additional information

Supplementary information The online version contains supplementary material available at <https://doi.org/10.1038/s41467-025-66965-5>.

Correspondence and requests for materials should be addressed to Jiafeng Ruan, Dalin Sun or Fei Wang.

Peer review information *Nature Communications* thanks Jiarui He, and the other, anonymous, reviewer(s) for their contribution to the peer review of this work. A peer review file is available.

Reprints and permissions information is available at <http://www.nature.com/reprints>

Publisher's note Springer Nature remains neutral with regard to jurisdictional claims in published maps and institutional affiliations.

Open Access This article is licensed under a Creative Commons Attribution-NonCommercial-NoDerivatives 4.0 International License, which permits any non-commercial use, sharing, distribution and reproduction in any medium or format, as long as you give appropriate credit to the original author(s) and the source, provide a link to the Creative Commons licence, and indicate if you modified the licensed material. You do not have permission under this licence to share adapted material derived from this article or parts of it. The images or other third party material in this article are included in the article's Creative Commons licence, unless indicated otherwise in a credit line to the material. If material is not included in the article's Creative Commons licence and your intended use is not permitted by statutory regulation or exceeds the permitted use, you will need to obtain permission directly from the copyright holder. To view a copy of this licence, visit <http://creativecommons.org/licenses/by-nc-nd/4.0/>.

© The Author(s) 2025

Acknowledgements

This work was financially supported by the National Key R&D Program of China (No. 2021YFA1201900; Fei W.), National Science Foundation of